

Predicting magnetism with first-principles AI

Max Geier and Liang Fu

Department of Physics, Massachusetts Institute of Technology, Cambridge, MA 02139, USA

(Dated: February 11, 2026)

Computational discovery of magnetic materials remains challenging because magnetism arises from the competition between kinetic energy and Coulomb interaction that is often beyond the reach of standard electronic-structure methods. Here we tackle this challenge by directly solving the many-electron Schrödinger equation with neural-network variational Monte Carlo, which provides a highly expressive variational wavefunction for strongly correlated systems. Applying this technique to transition metal dichalcogenide moiré semiconductors, we predict itinerant ferromagnetism in WSe₂/WS₂ and an antiferromagnetic insulator in twisted Γ -valley homobilayer, using the same neural network without any physics input beyond the microscopic Hamiltonian. Crucially, both types of magnetic states are obtained from a single calculation within the $S_z = 0$ sector, removing the need to compute and compare multiple S_z sectors. This significantly reduces computational cost and paves the way for faster and more reliable magnetic material design.

Introduction.— Magnets play a key role in modern technology – powering permanent-magnet motors in vehicles, turbines, and robots, and enabling magnetic data storage and emerging spintronic functionality. Today’s highest-performance permanent magnets, NdFeB and SmCo, rely on rare-earth elements, whose limited availability motivates the search for rare-earth-free alternatives and new design principles. At a fundamental level, magnetism is intrinsically quantum: a classical many-particle system in equilibrium has zero magnetization even in the presence of an external magnetic field [1–3]. Instead, magnetism largely arises from long-range order of electron’s spin, driven by spin-independent Coulomb repulsion and kinetic energy – whereas direct magnetic dipole–dipole couplings are usually negligible [4].

The energy scale of magnetic ordering—as indicated by the Curie or Néel temperature—is typically much smaller than the Coulomb and kinetic energy scale. In metals, ferromagnetic ordering depends on the delicate balance between kinetic and interaction energies, and is often strongly influenced by exchange–correlation effects. In antiferromagnetic insulators, the ordering is often controlled by small kinetic-exchange (superexchange) couplings arising from virtual hopping between localized orbitals. As a result, it is difficult to predict magnetism reliably by solving many-electron Schrödinger equation with standard electronic-structure methods such as density functional theory or Hartree-Fock theory. As a paradigmatic example, it remains debated whether the uniform electron gas exhibits a ferromagnetic metal phase [5, 6].

Recently, neural networks have emerged as a powerful tool for constructing many-electron variational wavefunctions in continuous space [7–11]. Importantly, unlike handcrafted trial wavefunctions that are task specific, a *single* neural network with a large number of trainable parameters can accurately find a vast variety of ground states—including metallic, insulating, superconducting and topologically ordered states—purely through unsupervised energy minimization [12–17], without pre-knowledge or physics-informed initialization. Moreover,

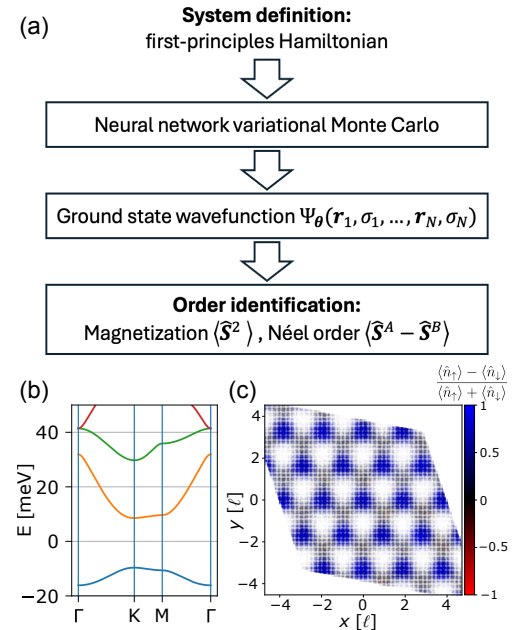


FIG. 1. (a) **Workflow.** Defining the quantum system with its first-principles Hamiltonian, the NNVNC technique optimizes a neural network to represent its ground state by energy minimization. The total magnetization $\langle \hat{S}^2 \rangle$ and staggered magnetization $\langle \langle \hat{S}^A - \hat{S}^B \rangle \rangle$ identifies the magnetic order of the ground state. (b) Band structure of the moiré semiconductor model for WSe₂/WS₂. (c) Spin density in the itinerant ferromagnetic state obtained from the variational solution with 28 electrons in 21 unit cells, for visualization shown for the $S_z = 7\hbar$ result where magnetization is aligned with the computational S_z basis. Color indicates spin polarization $\langle \hat{n}_\uparrow \rangle - \langle \hat{n}_\downarrow \rangle$ and opacity total density $\langle \hat{n}_\uparrow \rangle + \langle \hat{n}_\downarrow \rangle$.

certain fermionic network architectures have been mathematically proven to be universal, that is, capable of approximating any continuous wavefunctions to arbitrary accuracy at sufficient network size [18, 19]. Neural-network variational Monte Carlo studies have achieved impressive success on several correlated electron systems

in real materials [20–26].

In this work, we develop a neural-network variational Monte Carlo (NN-VMC) method to predict magnetism from first-principles by solving the many-electron Schrödinger equation directly. By allowing for general spin dependence in the wavefunction $\Psi(\mathbf{r}_1, \sigma_1, \dots, \mathbf{r}_N, \sigma_N)$, our fermionic network is capable of solving non-magnetic, ferromagnetic and antiferromagnetic ground states on equal footing in $SU(2)$ -spin rotation invariant systems. Our method eliminates the need of solving separately and comparing states of different magnetization, thus reducing the computational cost and attaining high accuracy.

We apply our first-principles neural-network method to study magnetism in two-dimensional Coulomb electron gas with a long-wavelength periodic potential. Such system is naturally realized in semiconductor moiré heterostructures such as WSe₂/WS₂ and twisted Γ -valley homobilayers such as WS₂, MoS₂, MoSe₂ [27, 28]. Our unbiased calculations predict metallic ferromagnet in the heterobilayer WSe₂/WS₂ and insulating antiferromagnet phases in homobilayers, depending on the filling factor.

Identifying magnetism.— For a $SU(2)$ -symmetric electronic Hamiltonian, the spin operators commute with the Hamiltonian $[\hat{H}, \hat{\mathbf{S}}^2] = [\hat{H}, \hat{S}_z] = 0$, so that eigenstates can be labeled by total spin $S^2 = \langle \hat{\mathbf{S}}^2 \rangle$ and its component S_z along the z direction. As a consequence, any ground state with total magnetization $S > 0$ appears as an $(2S + 1)$ -fold degenerate multiplet with identical energy for all S_z sectors with $|S_z| \leq S$. This provides a direct, symmetry-based definition of magnetism: A system has a ferromagnetic ground state if it has total magnetization $\langle \hat{\mathbf{S}}^2 \rangle > 0$, which manifests as a degeneracy and equal total spin S observed across all sectors with $|S_z| \leq S$.

Importantly, all possible total magnetization states $\langle \hat{\mathbf{S}}^2 \rangle \in [0, \frac{N}{2}(\frac{N}{2} + 1)]$, where N is the number of electrons, can be realized in the $S_z = 0$ sector. Therefore, solving for the lowest-energy in the $S_z = 0$ sector identifies the ground state independent on its total magnetization $\langle \hat{\mathbf{S}}^2 \rangle$. Practically however, reaching a finite magnetization $\langle \hat{\mathbf{S}}^2 \rangle > 0$ in the $S_z = 0$ requires that the numerical method is capable to express and reach a finite in-plane magnetization. Representing such spin-states is challenging for traditional numerical methods, and it is not *a priori* clear whether a variational numerical technique can efficiently represent and *autonomously* identify such states. Remarkably, our results below show that the NN-VMC technique identifies the fully spin-polarized state $\langle \hat{\mathbf{S}}^2 \rangle = S(S + 1)\hbar^2$ already within the $S_z = 0$ sector purely by energy minimization. This demonstrates that the approach is sufficiently expressive to identify magnetism from a *single* calculation at $S_z = 0$.

Neural Network Wavefunction and Variational Monte Carlo.— We employ a neural-network parameterization of the many-electron wavefunction within variational

Monte Carlo to solve the continuum Schrödinger equation by direct energy minimization. The wavefunction is represented as a sum of K determinants of generalized orbitals,

$$\Psi(\mathbf{x}_1, \dots, \mathbf{x}_N) = \sum_{k=1}^K \det_{ij} \phi_j^k(\mathbf{x}_i, \mathbf{x}_{/i}), \quad (1)$$

where $\mathbf{x}_i = (\mathbf{r}_i, \sigma_i)$ denotes the position \mathbf{r}_i and spin σ_i of electron i . The generalized orbitals $\phi_j^k(\mathbf{x}_i; \mathbf{x}_{/i})$ explicitly encode many-body correlations by allowing the orbital of electron i to depend on the configuration of all other electrons. The key advantage of this approach is that Eq. (1) yields a flexible amplitude and nodal structure which can *universally* represent two-dimensional fermionic wavefunctions using only a few determinants [18, 19]. Notably, the joint embedding of electron coordinate and spin—treated on equal footing—allows for spinful generalized orbitals in general form [29]. These orbitals in Eq. (1) are constructed using a transformer neural network, which is a universal approximator of permutation-equivariant sequence-to-sequence ($\{\mathbf{x}_i\} \rightarrow \{\phi_j\}$) functions [30]. The detailed construction of the neural network wavefunction is contained in Refs. [10, 12].

We employ Markov-chain Monte-Carlo sampling [31] for the efficient numerical evaluation of energy expectation values and observables. We employ a Kroencker factored curvature approximation [32] in the gradient updates, which leads to faster and more stable convergence [7, 33, 34]. Hyperparameters and training details are summarized in the Supplementary Material. A detailed description of the variational Monte Carlo technique is contained in Refs. [7, 12, 31] and peculiarities to spinful systems are discussed in Refs. [25, 29, 35–42].

System.— In this work, we explore magnetism in two-dimensional semiconductor moiré materials. The first system of our study is doped WSe₂/WS₂, described by a continuum Hamiltonian [43, 44]:

$$H = \sum_i \left(-\frac{\hbar^2}{2m^*} \nabla_i^2 + V(\mathbf{r}_i) \right) + \frac{1}{2} \sum_i \sum_{i \neq j} \frac{e^2}{4\pi\epsilon\epsilon_0 |\mathbf{r}_i - \mathbf{r}_j|}, \quad (2)$$

where $V(\mathbf{r}) = -2V \sum_{j=1}^3 \cos(\mathbf{g}_j \cdot \mathbf{r} + \varphi)$ is the moiré potential with reciprocal lattice vectors $\mathbf{g}_j = \frac{4\pi}{\sqrt{3}a_M} (\cos \frac{2\pi j}{3}, \sin \frac{2\pi j}{3})$, moiré lattice constant a_M , and φ controls the shape of the moiré potential. This continuum Hamiltonian describes interacting electrons in a long-wavelength periodic potential arising from the moiré superlattice. A wide variety of emergent quantum phases has been studied in this moiré platform [45–50], including Mott insulators, generalized Wigner crystals, and electron stripes.

So far metallic ferromagnetism has been theoretically predicted and experimentally observed in twisted bilayer transition metal dichalcogenides (TMDs) [51, 52], which

hosts a pair of Chern bands with opposite Chern numbers for $s_z = \pm 1/2$ electrons. In contrast, the continuum Hamiltonian (2) for WSe₂/WS₂ and similar TMD heterobilayers does not support topological bands and exhibits SU(2) spin symmetry. For this class of moiré semiconductors, previous studies [53–59] have proposed kinetic mechanism for itinerant ferromagnetism based on a simplified Hubbard model description. However, a quantitatively accurate prediction from solving the first-principles interacting Hamiltonian has been lacking.

We search for itinerant magnetism in WSe₂/WS₂ bilayers using model parameters extracted from large-scale DFT calculations: effective mass $m^* = 0.5 m_e$, moiré lattice constant $a_M = 8.2$ nm, moiré potential strength $V = 15$ meV, shape $\varphi = \pi/4$, and dielectric constant of the surrounding hBN insulator $\epsilon = 6$ [44].

Itinerant magnetism.— The typical interaction strength $\frac{e^2}{4\pi\epsilon\epsilon_0\ell} = 56.9$ meV is large compared to the band width of the lowest energy band [Fig. 1(b)] as well as the spacing to the next excited bands. Here the length scale $\ell = a_M/\sqrt{2\pi/\sqrt{3}} = 4.31$ nm is average interparticle distance at density close to one electron per unit cell. Therefore both electron-correlation effects and interaction-induced mixing between bands are strong. As a consequence, this realistic system is not amenable to standard numerical treatments, which typically rely on projection of the full Hamiltonian to the lowest-energy band. In contrast, our first-principles neural network method operates directly in continuum real-space and thereby fully captures interaction-induced band-mixing – which is important for quantitatively accurate predictions.

As evidence of the magnetized ground state, we solve by direct energy minimization for the ground state in all S_z sectors. Fig. 2(a) and (b) show the final energy and magnetization $\langle \hat{S}^2 \rangle$ in a system with 21 unit cells and 28 particles. For $|S_z| \leq 7\hbar$, the ground state energies are approximately degenerate, and all states reach approximately the total magnetization $\langle \hat{S}^2 \rangle = 56\hbar^2$. This matches the expectation for a ferromagnetic state with total spin $S = 7\hbar$ and magnetization $\langle \hat{S}^2 \rangle = S(S+1) = 56\hbar^2$. Remarkably, the ferromagnetic state is already identified from the calculation at $S_z = 0$. This demonstrates that the method is sufficiently accurate and expressive to learn the magnetized state even when restricting to the $S_z = 0$ sector.

To pin down the nature of the partially-polarized state, we compute the total occupation $\sum_\alpha \langle c_{\mathbf{k},\alpha,\sigma}^\dagger c_{\mathbf{k},\alpha,\sigma} \rangle$ summed over bands α and resolved by momenta \mathbf{k} within the first Brillouin zone and spin σ [Fig. 2(c) and (d)]. While the occupation of the dominant spin \uparrow is uniform throughout the Brillouin zone [Fig. 2(c)], the minority spin \downarrow is partially occupied around the center of the Brillouin zone [Fig. 2(d)]. This minimizes the kinetic energy of the minority spin: The occupied momenta have minimal energy in the corresponding band structure shown

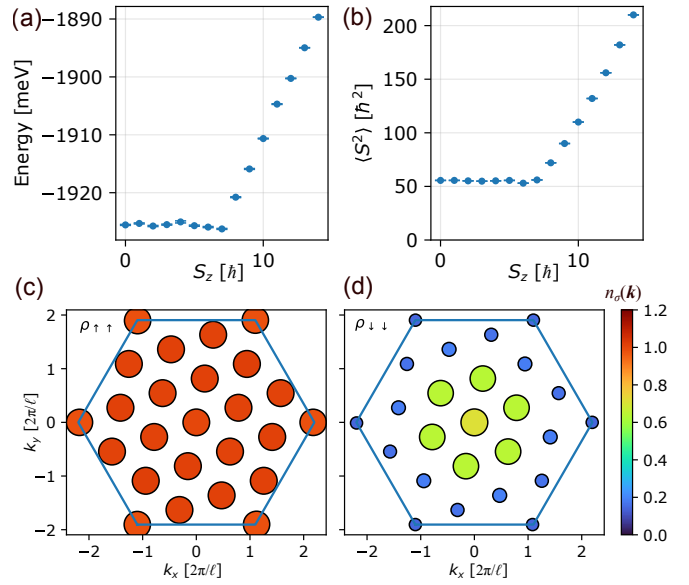


FIG. 2. **Itinerant magnetism.** (a) Ground state energy in different S_z sectors and (b) total spin $\langle \hat{S}^2 \rangle$ in different S_z sectors in the model for WSe₂/WS₂ semiconductor with 28 particles in 21 unit cells. Panels (c) and (d) show the total occupation $n_\sigma(\mathbf{k}) = \sum_\alpha \langle c_{\mathbf{k},\alpha,\sigma}^\dagger c_{\mathbf{k},\alpha,\sigma} \rangle$ of modes resolved by spin σ and momentum \mathbf{k} quantum numbers in the first Brillouin zone, visualized for the $S_z = 7\hbar$ sector. For visualization, we included the values at all K points on the first Brillouin zone corners.

in Fig. 1(b). The partial filling within a sharp Fermi sea of the minority spin band indicates that the state is metallic.

Direct evidence of metallic ferromagnetism in WSe₂/WS₂ has not yet been experimentally observed. Encouragingly, magnetic circular dichroism data [60] shows a Curie-Weiss like temperature dependence, with a positive Weiss constant indicating possible ferromagnetism at filling fractions $\nu \in [1.2, 1.4]$. This is consistent with our finding of the ferromagnetic ground state at filling fraction $\nu = 4/3$ reported here.

Antiferromagnetism.— In a SU(2)-symmetric system, Néel antiferromagnetism has zero net magnetization $\langle \hat{S}^2 \rangle = 0$, instead it exhibits a finite staggered magnetic polarization $\langle \hat{S}^A - \hat{S}^B \rangle > 0$, where $\hat{S}^{A/B}$ is the total magnetization of electrons restricted to sublattice regions A/B.

We search for antiferromagnetism in moiré semiconductors that naturally realize a long-wavelength honeycomb lattice: twisted transition metal dichalcogenide bilayers where low-energy bands are derived from interlayer hybridized Γ -valley states [27, 28]. This class of systems has typically a large effective mass $m^* \approx m_e$ and hybridization moiré potential strength of 10 to 20 meV [27, 28]. In the following we use as default parameters the effective mass $m^* = m_e$, moiré potential strength $V = 15$ meV, shape $\varphi = \pi$, dielectric constant

of the surrounding insulator $\epsilon = 6$, and moire lattice constant $a_M = 6$ nm which corresponds to a twist angle of $\theta = 3.00^\circ$ using the typical monolayer lattice constant of 3.15 \AA .

In this parameter regime, the honeycomb moiré modulation produces narrow minibands with bandwidth of a few tens of meV [Fig. 3(a)], which is comparable to the typical interaction strength $\frac{e^2}{4\pi\epsilon\epsilon_0\ell} = 76$ meV. We consider the filling of two electrons per unit cell, so that in the noninteracting case, the lowest-energy band is fully filled up to the symmetry-enforced Dirac cone at the K points. In the opposite regime of strong interaction, each sublattice of the honeycomb potential localizes an electron, and kinetic superexchange neighboring A/B sites leads to an antiferromagnetic ordering.

For the realistic material parameters used here, this Néel antiferromagnetic order is discovered in the ground state obtained from the NN-VMC optimization: the real-space spin polarization $\langle n_\uparrow(\mathbf{r}) - n_\downarrow(\mathbf{r}) \rangle$ alternates between the two sublattices [Fig. 3(b)]. To quantify the onset and strength of antiferromagnetism we evaluate the staggered order parameter

$$M_z = \langle S_z^A - S_z^B \rangle, \quad (3)$$

where $S_z^{A/B}$ denotes the total spin within the two moiré sublattice regions A/B. Figure 3(c) shows M_z as a function of moiré potential strength V at fixed interaction strength: increasing V localizes carriers within the moiré unit cell, reduces the effective bandwidth, and drives a rapid growth of Néel correlations. The sudden jump from $M_z = 0$ to a finite value at $V_c = 7.7$ meV indicates a correlation-driven transition from a paramagnetic metal into a robust antiferromagnetic state.

Finally, we distinguish an antiferromagnetic insulator from an antiferromagnetic metal by examining the small- q behavior of the static structure factor [Fig. 3(d)]. Plotting $4\pi S(q)/q^2$ highlights the long-wavelength response: an insulating state exhibits a finite $q \rightarrow 0$ limit (incompressible, gapped charge sector), while a divergence as $q \rightarrow 0$ signals a gapless, metallic response [61–64]. At small $V < V_c$, the static structure factor indicates a metallic state while for $V \gg V_c$ the data indicates insulating behavior. This result is consistent with the fact that Néel order parameters opens up an energy gap at the Dirac points.

Discussion.— Our results show that the NN-VMC technique can reliably and autonomously solve magnetic phases that emerge from the interplay of Pauli principle and Coulomb interactions. Because the method operates directly in the continuum and is systematically improvable through the neural network dimensions and optimization effort, it enables quantitatively accurate predictions of magnetism in realistic material models. Importantly, our results demonstrate that the approach autonomously identifies the magnetized state in the $S_z = 0$ sector – eliminating the need to compare calculations

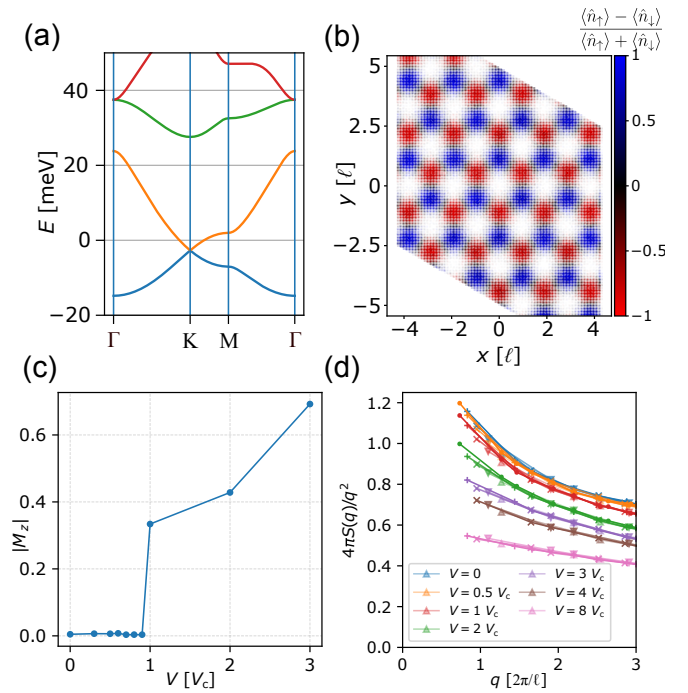


FIG. 3. **Antiferromagnetic insulator.** (a) Band structure and (b) spin density for the homobilayer semiconductor model with honeycomb potential $\varphi = \pi$, Eq. (2), for $V = 15$ meV, $\epsilon = 6$, and 54 electrons. (c) Staggered magnetization $M_z = \langle S_z^A - S_z^B \rangle$ as a function of potential strength computed for 18 electrons in 9 unit cells. (d) Long-wavelength behavior of the static structure factor $4\pi S(q)/q^2$ for different potential strength V computed for variable system sizes of 9 (“ \triangle ”), 12 (“ ∇ ”), 16 (“ \times ”), 21 (“ $+$ ”), and 27 (“ \cdot ”) unit cells and two electrons per unit cell, with $V_c = 7.7$ meV.

from different spin sectors.

More broadly, accurately describing spin effects is essential across chemistry, biophysics, and quantum materials, because key functionalities are often controlled by competing spin states. In chemical reactions, multiple spin-resolved potential-energy surfaces compete and the ground spin state can change during bond stretching – so that the resulting forces are highly sensitive to the spin state during the reaction [65–67]. As a concrete example, in transition-metal catalysis, multiple spin states can lie close in energy, and changes in the transition-metal spin state can substantially modify activation barriers and selectivity [68, 69]. In drug metabolism by cytochrome P450 enzymes, substrate binding induces spin shifts in the heme iron, which changes reduction potential and thereby oxygen activation and selectivity [70–73]. In the cuprate high-temperature superconductors, kinetic superexchange between spins is a key contributor to the Cooper pairing [74]. Since standard electronic-structure methods can struggle precisely in these regimes of strong correlation and competing spin states [75, 76], our ability to recover magnetic ground states from the continuum many-electron problem supports NN-VMC as a promis-

ing route toward more predictive simulations in a wide range of spinful systems.

Acknowledgements.— MG and LF were supported by a Simons Investigator Award from the Simons Foundation. This work made use of computing resources provided by the National Science Foundation under Cooperative Agreement PHY-2019786 (The NSF AI Institute for Artificial Intelligence and Fundamental Interactions).

Code availability.— The numerical calculations in this work are based on our public codebase `PeriodicWave` [77], described in Ref. [12].

Data availability.— The data required to reproduce and benchmark the numerical results, specifically the ground state energies of the wavefunctions used to generate the numerical results in Fig. 2 and 3, are contained in the Supplementary Material.

[1] N. Bohr, *Studier over metallernes elektrontheori* (Thaning & Appel in Komm., 1911).

[2] H. J. Van Leeuwen, *Vraagstukken uit de electronentheorie van het magnetisme* (Eduard Ijdo, 1919).

[3] J. H. Van Vleck, *The theory of electric and magnetic susceptibilities* (Oxford University Press, 1932).

[4] D. Vollhardt, N. Blümer, K. Held, and M. Kollar, *Metallic ferromagnetism - an electronic correlation phenomenon* (2000), arXiv:cond-mat/0012203 [cond-mat.str-el].

[5] N. D. Drummond and R. J. Needs, Phase diagram of the low-density two-dimensional homogeneous electron gas, *Phys. Rev. Lett.* **102**, 126402 (2009).

[6] C. Smith, Y. Chen, R. Levy, Y. Yang, M. A. Morales, and S. Zhang, Unified variational approach description of ground-state phases of the two-dimensional electron gas, *Phys. Rev. Lett.* **133**, 266504 (2024).

[7] D. Pfau, J. S. Spencer, A. G. D. G. Matthews, and W. M. C. Foulkes, Ab initio solution of the many-electron Schrödinger equation with deep neural networks, *Phys. Rev. Res.* **2**, 033429 (2020).

[8] J. Hermann, Z. Schätzle, and F. Noé, Deep-neural-network solution of the electronic Schrödinger equation, *Nat. Chem.* **12**, 891 (2020).

[9] K. Choo, A. Mezzacapo, and G. Carleo, Fermionic neural-network states for ab-initio electronic structure, *Nat. Commun.* **11**, 1 (2020).

[10] I. von Glehn, J. S. Spencer, and D. Pfau, A self-attention ansatz for ab-initio quantum chemistry, in *The Eleventh International Conference on Learning Representations* (2023).

[11] G. Pescia, J. Nys, J. Kim, A. Lovato, and G. Carleo, Message-passing neural quantum states for the homogeneous electron gas, *Physical Review B* **110**, 035108 (2024).

[12] M. Geier, K. Nazaryan, T. Zaklama, and L. Fu, Self-attention neural network for solving correlated electron problems in solids, *Phys. Rev. B* **112**, 045119 (2025).

[13] Y. Teng, D. D. Dai, and L. Fu, Solving the fractional quantum Hall problem with self-attention neural network, *Phys. Rev. B* **111**, 205117 (2025).

[14] C.-T. Li, T. Ong, M. Geier, H. Lin, and L. Fu, *Attention is all you need to solve chiral superconductivity* (2025), arXiv:2509.03683 [cond-mat.supr-con].

[15] F. Gaggioli, P.-A. Graham, and L. Fu, *Electronic crystals and quasicrystals in semiconductor quantum wells: an ai-powered discovery* (2025), arXiv:2512.10909 [cond-mat.str-el].

[16] A. Abouelkomsan, M. Geier, and L. Fu, *Topological order in deep state* (2025), arXiv:2512.01863 [cond-mat.mes-hall].

[17] A. Abouelkomsan and L. Fu, *First-principles ai finds crystallization of fractional quantum hall liquids* (2026), arXiv:2602.03927 [cond-mat.mes-hall].

[18] L. Fu, *A minimal and universal representation of fermionic wavefunctions (fermions = bosons + one)* (2025), arXiv:2510.11431 [cond-mat.str-el].

[19] L. Fu, *Fermi sets: Universal and interpretable neural architectures for fermions* (2026), arXiv:2601.02508 [cond-mat.str-el].

[20] X. Li, Z. Li, and J. Chen, *Ab initio calculation of real solids via neural network ansatz*, *Nat. Commun.* **13**, 1 (2022).

[21] G. Cassella, H. Sutterud, S. Azadi, N. D. Drummond, D. Pfau, J. S. Spencer, and W. M. C. Foulkes, *Discovering Quantum Phase Transitions with Fermionic Neural Networks*, *Phys. Rev. Lett.* **130**, 036401 (2023).

[22] D. Lintneau, S. Moroni, G. Carleo, and M. Holzmann, *Neural wave functions for high-pressure atomic hydrogen* (2025), arXiv:2504.07062 [cond-mat.str-el].

[23] X. Li, Y. Chen, B. Li, H. Chen, F. Wu, J. Chen, and W. Ren, *Deep learning sheds light on integer and fractional topological insulators* (2025), arXiv:2503.11756 [cond-mat.str-el].

[24] X. Li, Y. Qian, W. Ren, Y. Xu, and J. Chen, *Emergent wigner phases in moirésuperlattice from deep learning*, *Communications Physics* **8**, 364 (2025).

[25] D. Luo, T. Zaklama, and L. Fu, *Solving fractional electron states in twisted MoTe₂ with deep neural network*, arXiv preprint arXiv:2503.13585 (2025).

[26] A. P. Fadon, D. Pfau, J. S. Spencer, W. T. Lou, T. Neupert, and W. M. C. Foulkes, *Extracting anyon statistics from neural network fractional quantum hall states* (2025), arXiv:2512.15872 [cond-mat.str-el].

[27] M. Angeli and A. H. MacDonald, Γ valley transition metal dichalcogenide moiré bands, *Proceedings of the National Academy of Sciences* **118**, e2021826118 (2021), <https://www.pnas.org/doi/pdf/10.1073/pnas.2021826118>.

[28] Y. Zhang, T. Liu, and L. Fu, *Electronic structures, charge transfer, and charge order in twisted transition metal dichalcogenide bilayers*, *Phys. Rev. B* **103**, 155142 (2021).

[29] A. Avdoshkin, M. Geier, and L. Fu, *A neural solver for spinful fermi systems* (2025), arXiv:2509.XXXXX [cond-mat.supr-con].

[30] C. Yun, S. Bhojanapalli, A. S. Rawat, S. Reddi, and S. Kumar, *Are transformers universal approximators of sequence-to-sequence functions?*, in *International Conference on Learning Representations* (2020).

[31] W. M. C. Foulkes, L. Mitas, R. J. Needs, and G. Ra-

jagopal, Quantum Monte Carlo simulations of solids, *Rev. Mod. Phys.* **73**, 33 (2001).

[32] J. Martens and R. Gross, Optimizing neural networks with kronecker-factored approximate curvature, in *Proceedings of the 32nd International Conference on International Conference on Machine Learning - Volume 37*, ICML'15 (JMLR.org, 2015) p. 2408–2417.

[33] A. Chen and M. Heyl, Empowering deep neural quantum states through efficient optimization, *Nature Physics* **20**, 1476 (2024).

[34] G. Goldshlager, N. Abrahamsen, and L. Lin, A kaczmarz-inspired approach to accelerate the optimization of neural network wavefunctions, *Journal of Computational Physics* **516**, 113351 (2024).

[35] K. Schmidt and S. Fantoni, A quantum monte carlo method for nucleon systems, *Physics Letters B* **446**, 99 (1999).

[36] A. Ambrosetti, P. L. Silvestrelli, F. Toigo, L. Mitas, and F. Pederiva, Variational monte carlo for spin-orbit interacting systems, *Phys. Rev. B* **85**, 045115 (2012).

[37] C. A. Melton, M. C. Bennett, and L. Mitas, Quantum Monte Carlo with variable spins, *The Journal of Chemical Physics* **144**, 244113 (2016).

[38] C. A. Melton, M. Zhu, S. Guo, A. Ambrosetti, F. Pederiva, and L. Mitas, Spin-orbit interactions in electronic structure quantum Monte Carlo methods, *Phys. Rev. A* **93**, 042502 (2016).

[39] C. Adams, G. Carleo, A. Lovato, and N. Rocco, Variational Monte Carlo calculations of $A \leq 4$ nuclei with an artificial neural-network correlator ansatz, *Physical Review Letters* **127**, 022502 (2021).

[40] L. Gerard, M. Scherbala, H. Sutterud, M. Foulkes, and P. Grohs, *Transferable Neural Wavefunctions for Solids* (2024), arXiv:2405.07599 [physics.comp-ph].

[41] X. Li, Y. Chen, B. Li, H. Chen, F. Wu, J. Chen, and W. Ren, Deep Learning Sheds Light on Integer and Fractional Topological Insulators, arXiv preprint arXiv:2503.11756 (2025).

[42] N. Zhan, W. A. Wheeler, E. Ertekin, R. P. Adams, and L. K. Wagner, Expressivity of determinantal ansatzes for neural network wave functions, arXiv preprint arXiv:2506.00155 (2025).

[43] F. Wu, T. Lovorn, E. Tutuc, and A. H. MacDonald, Hubbard model physics in transition metal dichalcogenide moiré bands, *Phys. Rev. Lett.* **121**, 026402 (2018).

[44] Y. Zhang, N. F. Q. Yuan, and L. Fu, Moiré quantum chemistry: Charge transfer in transition metal dichalcogenide superlattices, *Phys. Rev. B* **102**, 201115 (2020).

[45] E. C. Regan, D. Wang, C. Jin, M. I. Bakti Utama, B. Gao, X. Wei, S. Zhao, W. Zhao, Z. Zhang, K. Yumigeta, *et al.*, Mott and generalized wigner crystal states in wse2/ws2 moiré superlattices, *Nature* **579**, 359 (2020).

[46] Y. Tang, L. Li, T. Li, Y. Xu, S. Liu, K. Barmak, K. Watanabe, T. Taniguchi, A. H. MacDonald, J. Shan, and K. F. Mak, Simulation of Hubbard model physics in WSe₂/WS₂ moiré superlattices, *Nature* **579**, 353 (2020).

[47] C. Jin, Z. Tao, T. Li, Y. Xu, Y. Tang, J. Zhu, S. Liu, K. Watanabe, T. Taniguchi, J. C. Hone, L. Fu, J. Shan, and K. F. Mak, Stripe phases in WSe₂/WS₂ moiré superlattices, *Nature Materials* **20**, 940 (2021).

[48] Y. Zhang, H. Isobe, and L. Fu, Density functional approach to correlated moire states: itinerant magnetism (2020), arXiv:2005.04238 [cond-mat.str-el].

[49] A. P. Reddy, T. Devakul, and L. Fu, Artificial Atoms, Wigner Molecules, and an Emergent Kagome Lattice in Semiconductor Moiré Superlattices, *Phys. Rev. Lett.* **131**, 246501 (2023).

[50] B. Padhi, R. Chitra, and P. W. Phillips, Generalized Wigner crystallization in moiré materials, *Physical Review B* **103**, 125146 (2021).

[51] V. Crépel and L. Fu, Anomalous hall metal and fractional chern insulator in twisted transition metal dichalcogenides, *Phys. Rev. B* **107**, L201109 (2023).

[52] E. Anderson, F.-R. Fan, J. Cai, W. Holtzmann, T. Taniguchi, K. Watanabe, D. Xiao, W. Yao, and X. Xu, Programming correlated magnetic states with gate-controlled moiré geometry, *Science* **381**, 325 (2023).

[53] M. Davydova, Y. Zhang, and L. Fu, Itinerant spin polaron and metallic ferromagnetism in semiconductor moiré superlattices, *Phys. Rev. B* **107**, 224420 (2023).

[54] L. Ciorciaro, T. Smoleński, I. Morera, N. Kiper, S. Hiesstand, M. Kroner, Y. Zhang, K. Watanabe, T. Taniguchi, E. Demler, and A. İmamoğlu, Kinetic magnetism in triangular moiré materials, *Nature* **623**, 509 (2023).

[55] I. Morera, M. Kanász-Nagy, T. Smolenski, L. Ciorciaro, A. İmamoğlu, and E. Demler, High-temperature kinetic magnetism in triangular lattices, *Physical Review Research* **5**, L022048 (2023).

[56] K. Lee, P. Sharma, O. Vafek, and H. J. Changlani, Triangular lattice Hubbard model physics at intermediate temperatures, *Physical Review B* **107**, 235105 (2023).

[57] U. F. P. Seifert and L. Balents, Spin polarons and ferromagnetism in doped dilute moiré-mott insulators, *Physical Review Letters* **132**, 046501 (2024).

[58] D. Pereira and E. J. Mueller, Kinetic magnetism in the crossover between the square and triangular lattice Fermi-Hubbard models, *Physical Review B* **112**, 245120 (2025).

[59] P. Potasz, N. Morales-Durán, N. C. Hu, and A. H. MacDonald, Itinerant ferromagnetism in transition metal dichalcogenides moiré superlattices, *Physical Review B* **109**, 045144 (2024).

[60] Y. Tang, L. Li, T. Li, Y. Xu, S. Liu, K. Barmak, K. Watanabe, T. Taniguchi, A. H. MacDonald, J. Shan, and K. F. Mak, Simulation of hubbard model physics in wse2/ws2 moirésuperlattices, *Nature* **579**, 353 (2020).

[61] A. Bijl, The lowest wave function of the symmetrical many particles system, *Physica* **7**, 869 (1940).

[62] R. P. Feynman, Atomic theory of liquid helium near absolute zero, *Phys. Rev.* **91**, 1301 (1953).

[63] R. P. Feynman, Atomic theory of the two-fluid model of liquid helium, *Phys. Rev.* **94**, 262 (1954).

[64] R. Feynman, Chapter ii application of quantum mechanics to liquid helium (Elsevier, 1955) pp. 17–53.

[65] R. Poli and J. N. Harvey, Spin forbidden chemical reactions of transition metal compounds. new ideas and new computational challenges, *Chemical Society Reviews* **32**, 1 (2003).

[66] M. Fuchs, Y.-M. Niquet, X. Gonze, and K. Burke, Describing static correlation in bond dissociation by kohn-sham density functional theory, *The Journal of Chemical Physics* **122**, 10.1063/1.1858371 (2005).

[67] J. N. Harvey, Understanding the kinetics of spin-forbidden chemical reactions, *Physical Chemistry Chemical Physics* **9**, 331 (2007).

[68] J. N. Harvey, R. Poli, and K. M. Smith, Understanding the reactivity of transition metal complexes involving multiple spin states, *Coordination Chemistry Re-*

views [238-239](#), [347](#) (2003), theoretical and Computational Chemistry.

[69] A. Enríquez-Cabrera, Y. Lai, L. Salmon, L. Routaboul, and A. Boussekou, Spin-state effect on the efficiency of a post-synthetic modification reaction on a spin crossover complex, *Communications Chemistry* **8**, [47](#) (2025).

[70] D. Hamdane, H. Zhang, and P. Hollenberg, Oxygen activation by cytochrome p450 monooxygenase, *Photosynth Res* **98**, [657](#) (2008).

[71] E. M. Isin and F. P. Guengerich, Substrate binding to cytochromes p450., *Anal Bioanal Chem* **392**, [1019](#) (2008).

[72] J. Kirchmair, M. J. Williamson, J. D. Tyzack, L. Tan, P. J. Bond, A. Bender, and R. C. Glen, Computational prediction of metabolism: sites, products, sar, p450 enzyme dynamics, and mechanisms., *J Chem Inf Model* **52**, [617](#) (2012).

[73] M. Swart and M. Costas, *Spin states in biochemistry and inorganic chemistry: influence on structure and reactivity* (John Wiley & Sons, 2015).

[74] S. M. O'Mahony, W. Ren, W. Chen, Y. X. Chong, X. Liu, H. Eisaki, S. Uchida, M. H. Hamidian, and J. C. S. Davis, On the electron pairing mechanism of copper-oxide high temperature superconductivity, *Proceedings of the National Academy of Sciences* **119**, [e2207449119](#) (2022), <https://www.pnas.org/doi/pdf/10.1073/pnas.2207449119>.

[75] A. I. Krylov, The quantum chemistry of open-shell species, in *Reviews in Computational Chemistry* (John Wiley & Sons, Ltd, 2017) Chap. 4, pp. 151–224, <https://onlinelibrary.wiley.com/doi/pdf/10.1002/9781119356059.ch4>.

[76] P. Verma, Z. Varga, and D. G. Truhlar, Hyper open-shell excited spin states of transition-metal compounds: fef2, fef2···ethane, and fef2···ethylene, *The Journal of Physical Chemistry A* **122**, [2563](#) (2018).

[77] M. Geier and K. Nazaryan, *PeriodicWave* (2025).

Appendix A: Training details

The hyperparameters used for training our model are summarized in Tab. I.

Our neural network VMC implementation is based on Refs. [\[7, 10, 12\]](#) and our public codebase *PeriodicWave* [\[77\]](#). Specific details to our implementation are discussed in Ref. [\[12\]](#).

Our calculations for the ferromagnetic phase (Fig. 2) were performed without a Jastrow factor. For the calculations for the antiferromagnetic phase (Fig. 3), we used a simple Jastrow factor to enforce cusp conditions, as introduced in Ref. [\[10\]](#).

Appendix B: Supplemental numerical data

1. Spin density and density-density correlation

We include in Fig. 4 the spin polarization along the S_z axis of the itinerant ferromagnet, computed in the $S_z = 0$ sector. Because in this sector, the spin order does

Parameter	Value
Architecture	
Network layers	$L = 2$
Attention heads per layer	$N_{\text{heads}} = 4$
Attention dimension	$d_k = 32$
Value dimension	$d_v = 32$
Perceptron dimension	$d_{\text{model}} = 128$
# perceptrons per layer	2
Determinants	$K = 4$
Layer norm	True
Training	
Learning rate schedule	$\eta = \eta_0 \frac{2t}{t_d} \frac{1}{1+(t/t_d)^2}$
Local energy clipping	$\rho = 5.0$
Training: FM [Fig. 2]	
Training iterations	120,000
Learning rate	$\eta_0 = 0.03$
Learning rate delay	$t_0 = 3000$
Training: AFM [Fig. 3]	
Training iterations	150,000
Learning rate	$\eta_0 = 0.003$
Learning rate delay	$t_0 = 10000$
MCMC	
Batch size	1024
Initial move width	0.1
KFAC	
Norm constraint	1×10^{-3}
Damping	1×10^{-4}

TABLE I. Table of default hyperparameters used in our numerical calculations with the self-attention neural network. Both calculations for FM and AFM were run with the same hyperparameters, except the explicitly mentioned learning rate hyperparameters.

not align with the computational spin S_z basis, the spin polarization along the S_z -direction in Fig. 4 is close to zero.

We further remark that the spin polarization of the itinerant ferromagnetic state computed for the computational basis aligned with the magnetization, i.e. for $S_z = 7\hbar$, [Fig. 1(c) in the main text], displays a slightly negative spin density (slightly red regions) at the B (higher-energy) lattice sites of the charge-transfer moire potential.

Figure 5 shows the spin-resolved density-density correlation function for the itinerant ferromagnetic state. The data is consistent with a Fermi liquid ground state.

For completeness, we include in Fig. 6 the spin-resolved density-density correlation function for the antiferromag-

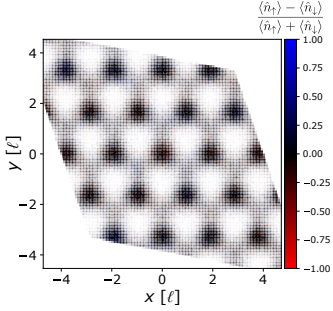


FIG. 4. Spin density along the S_z axis in the itinerant ferromagnet as discussed in Fig. 1(c) and Fig. 2 in the main text, computed in the $S_z = 0$ sector for the system with 28 electrons in 21 unit cells.

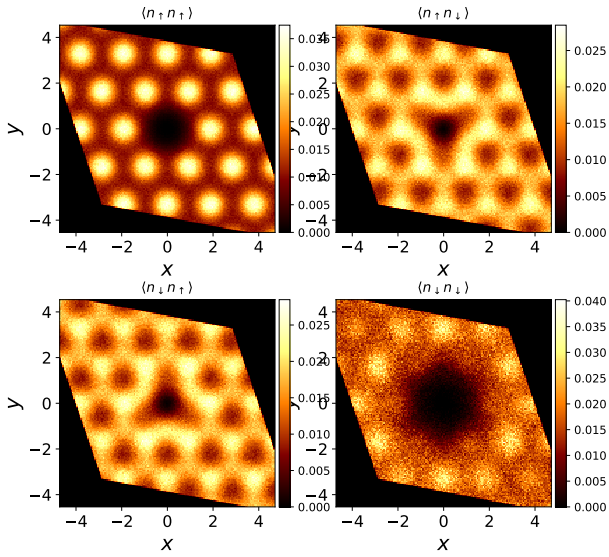


FIG. 5. Spin density-density correlation in the itinerant ferromagnet as discussed in Fig. 2 in the main text. The data shown here is computed from the system with 28 electrons in 21 unit cells at $S_z = 7\hbar$.

netic state at 54 particles.

2. Energies

We provide the ground state energies of our final wavefunctions used to generate the results shown in Fig. 2 and 3 in the main text for reproducibility and future benchmark.

In the numerical calculations, we convert SI units to

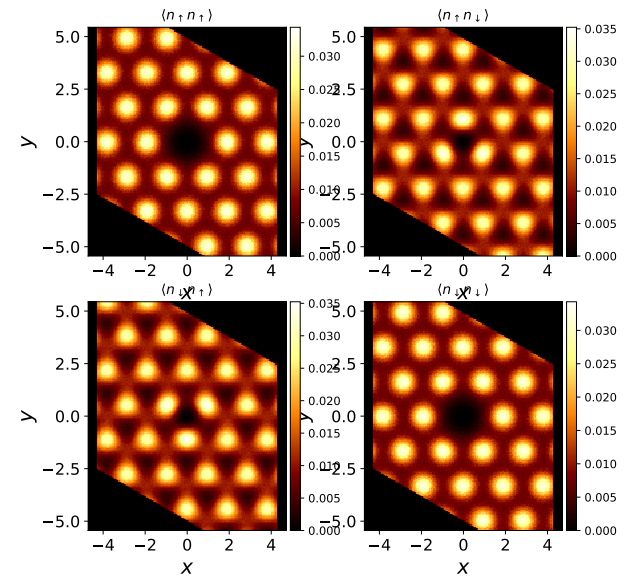


FIG. 6. Spin density-density correlation in the antiferromagnet as discussed in Fig. 3 in the main text. The data shown here is computed from the system with 54 electrons in 27 unit cells.

natural units and solve a Hamiltonian of the form

$$H = \sum_i \left(-\frac{1}{2} \nabla_i^2 + \tilde{V}(\mathbf{r}_i) \right) + \frac{1}{2} \sum_i \sum_{i \neq j} \frac{U}{|\mathbf{r}_i - \mathbf{r}_j|}, \quad (B1)$$

where $\tilde{V}(\mathbf{r}) = -2\tilde{V} \sum_{j=1}^3 \cos(\mathbf{g}_j \cdot \mathbf{r} + \varphi)$. Converting from SI to natural units of Eq. (B1), energies are measured in $\frac{2\pi}{\sqrt{3}} \frac{\hbar^2}{m^* a_M^2}$ and lengths in $\ell = a_M / \sqrt{2\pi/\sqrt{3}} = 4.31$ nm. In these units, the moire length is set to $\tilde{a}_M = \sqrt{2\pi/\sqrt{3}}$ so that the mean interparticle distance equals $1/\sqrt{\nu}$ where $\nu = N_{\text{el}}/N_{\text{uc}}$ is the filling fraction defined as the ratio of electron number by number of unit cells in the supercell.

For the itinerant magnet presented in the main text [Fig. 2] with $m^* = 0.5m_e$, potential strength $V = 15$ meV, dielectric constant $\epsilon = 6$, the energy scale is $\frac{2\pi}{\sqrt{3}} \frac{\hbar^2}{m^* a_M^2} = 8.22$ meV and length scale $\ell = a_M / \sqrt{2\pi/\sqrt{3}} = 4.31$ nm. Converting to natural units, the potential strength is $\tilde{V} = 1.82$ and the interaction strength $U = \ell/a_B^* = 6.78$ where $a_B^* = \frac{4\pi\epsilon\epsilon_0\hbar^2}{e^2 m^*} = 0.635$ nm is the effective Bohr radius. Table II contains the ground state energies and total spin of the data shown in Fig. 2.

For the antiferromagnetic model [Fig. 3], the default parameters are effective mass $m^* = m_e$, moire potential strength $V = 15$ meV, moire lattice constant $a_M = 6$ nm, and dielectric constant of the surrounding insulator $\epsilon =$

6. These translate to natural units $\tilde{V} = 2$, $U = 10$. The energy scale is $\frac{2\pi}{\sqrt{3}} \frac{\hbar^2}{m^* a_M^2} = 7.68$ meV. Table III contains the ground state energies of the wavefunctions used to generate the results for the antiferromagnetic model presented in Fig. 3 in the main text.

For accurate comparison for future benchmark, the direct energies in natural units as reported in Tabs. II and III should be used, not their conversion to meV, in order to avoid rounding errors in the unit conversion.

S_z	E	$SE(E)$	S^2	$SE(S^2)$
0	-234.198	0.010	55.586	0.018
1	-234.167	0.011	55.604	0.012
2	-234.221	0.011	55.193	0.011
3	-234.192	0.010	54.888	0.015
4	-234.135	0.022	55.211	0.013
5	-234.214	0.012	55.582	0.016
6	-234.243	0.011	53.020	0.015
7	-234.282	0.010	56.030	0.004
8	-233.616	0.009	72.023	0.003
9	-233.022	0.009	90.013	0.004
10	-232.384	0.008	110.025	0.003
11	-231.660	0.007	132.014	0.002
12	-231.121	0.006	156.002	0.003
13	-230.477	0.004	182.005	0.003
14	-229.835	0.002	210.000	0.000

TABLE II. Ground state energies and total magnetization obtained from the final wavefunction of the itinerant magnet shown in Fig. 2, for all S_z sectors, together with their standard error (SE). Here, energies are reported in natural units as obtained from Eq. (B1) with $\tilde{V} = 1.82$, $U = 6.78$, and for 28 electrons in 21 unit cells. The conversion factor to meV is 8.2219431 meV. Energies have been averaged over 512000 local energy evaluations.

N	\tilde{V}	E	$SE(E)$
18	0.0	-206.406	0.004
24	0.0	-274.401	0.005
32	0.0	-366.371	0.006
42	0.0	-479.894	0.006
18	0.5	-210.036	0.004
24	0.5	-278.726	0.004
32	0.5	-372.619	0.005
42	0.5	-487.981	0.006
54	0.5	-626.230	0.018
18	1.0	-218.666	0.005
24	1.0	-290.705	0.005
32	1.0	-388.177	0.007
42	1.0	-508.433	0.008
54	1.0	-653.501	0.017
18	2.0	-244.943	0.004
24	2.0	-326.166	0.005
32	2.0	-434.519	0.006
42	2.0	-570.319	0.008
54	2.0	-732.960	0.019
18	3.0	-277.319	0.003
24	3.0	-369.512	0.004
32	3.0	-492.320	0.006
42	3.0	-645.994	0.007
18	4.0	-312.571	0.003
24	4.0	-416.514	0.004
32	4.0	-555.057	0.006
18	8.0	-467.495	0.004
24	8.0	-623.499	0.005
32	8.0	-831.187	0.005
42	8.0	-1090.812	0.008

TABLE III. Ground state energies of the wavefunctions obtained for the antiferromagnetic system discussed in Fig. 3. The energies are given in natural units as in Eq. (B1). N is the total number of electrons. All data is computed for $U = 10$ and length scales so that the moiré period $a_M = \sqrt{2\pi/\sqrt{3}}$. The system size is chosen such that there are exactly two electrons per unit cell. The conversion factor to meV is 7.678381325 meV.